February 24, 2009 | vol. 106 | no. 8 | pp. 2473–2968

PNAS

Proceedings of the National Academy of Sciences of the United States of America www.pnas.org

Chirality controls nanotube growth

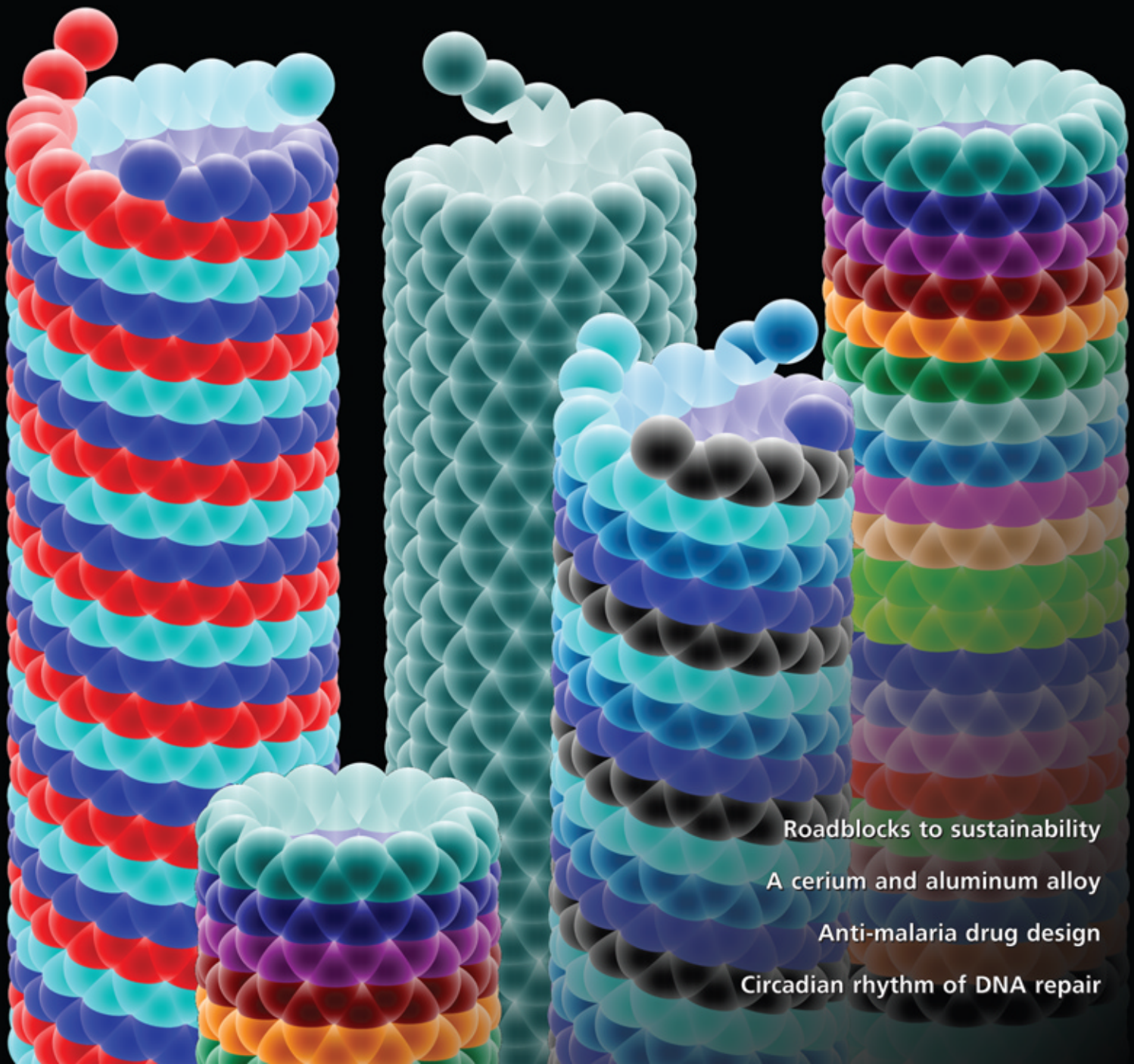

Roadblocks to sustainability

A cerium and aluminum alloy

Anti-malaria drug design

Circadian rhythm of DNA repair

Dislocation theory of chirality-controlled nanotube growth

Feng Ding[a], Avetik R. Harutyunyan[b], and Boris I. Yakobson[a,1]

[a]Department of Mechanical Engineering and Materials Science, and Department of Chemistry, Rice University, Houston, TX 77005; and [b]Honda Research Institute USA, Inc., Columbus, OH 43212

Communicated by Robert F. Curl, Jr., Rice University, Houston, TX, December 22, 2008 (received for review August 23, 2008)

The periodic makeup of carbon nanotubes suggests that their formation should obey the principles established for crystals. Nevertheless, this important connection remained elusive for decades and no theoretical regularities in the rates and product type distribution have been found. Here we contend that any nanotube can be viewed as having a screw dislocation along the axis. Consequently, its growth rate is shown to be proportional to the Burgers vector of such dislocation and therefore to the chiral angle of the tube. This is corroborated by the ab initio energy calculations, and agrees surprisingly well with diverse experimental measurements, which shows that the revealed kinetic mechanism and the deduced predictions are remarkably robust across the broad base of factual data.

carbon | catalysis | kinetics | nucleation | synthesis

Synthesis of carbon nanotubes (CNTs), traditionally referred to as "growth" due to their drawn-out crystal morphology, has been a great challenge for experiment and theory. They are produced in a seemingly random distribution of diameters and chiral symmetry, often specified by the angle θ between the circumference and the zigzag motif of atoms. Despite tremendous efforts (1–4), the growth mechanism remains unclear in significant details. Theory has been discussed mainly at the 2 distinct scales, continuum-phenomenological vapor-liquid-solid (VLS) model (5) and atomistic simulations (6–14). Here we invoke the concepts established for macroscopic crystals and transfer this to a nanotube viewing as having an axial screw dislocation. Following this logic further, we show that the growth rate must be proportional to the magnitude of the Burgers vector of such dislocation and is ultimately proportional to the chiral angle of the tube.

Despite its molecular size and round shape, a CNT possesses the attributes of an ideal crystal, as well as possible deviations in the form of defects (15). The notion of edge dislocation (5/7 defect) was first applied to CNTs in the context of mechanical relaxation and turned out rather useful, leading to an understanding of yield and superplasticity (16, 17). In the following, we invoke another fundamental dislocation type, the screw dislocation, and explore its utility in understanding CNT growth.

Results and Discussion

Our initial plan is to follow Frank's seminal work (18). It resolved the problem of crystal growth kinetics, where nucleating every next crystal plane on top of a previously completed one would encounter a significant barrier. Frank suggested that a screw dislocation provides a non-barrier path for the sequential accretion of material along the spiral ladder of a crystal lattice, so that the growing facet never becomes a complete low-index plane.

In this regard, the armchair and zigzag tubes are special: each of these achiral types represent a stack of complete atomic rings, so that the circular end-edge is entirely uniform (Fig. 1*A* illustrates the zigzag case), similar to a low-index crystal plane. Any chiral tube can be viewed as a basic zigzag, but with a "defect"—a running through the center-hollow screw dislocation of a Burgers vector **b** (Fig. 1*B-D*) (19). (The reason to choose the zigzag tube rather than armchair as a basic one will become clear later.) In a gedanken experiment, one dissects the wall of a zigzag tube axially (Fig. 1*B*) and then reseals the cut after sliding its sides by a vector $\mathbf{b} = \mathbf{b}_\gamma + \mathbf{b}_\perp$. Consequently, the tube end-edge gains a kink-step of height b_γ (or equivalently, a few smaller kinks). By inspection (*SI Text* and Fig. S1), we see that a CNT with conventional indices (n, m) corresponds to a purely zigzag (n + m/2, 0) with an axial screw dislocation "defect" of Burgers vector $\mathbf{b}_\gamma = m(-\frac{1}{2}, 1)$ [for an odd m, a purely zigzag tube ($n + m/2 + \frac{1}{2}$, 0) and additionally a small edge component $b_\perp = -\frac{1}{2}$, (Fig. S1)]; accordingly, its circular end-rim has m kinks

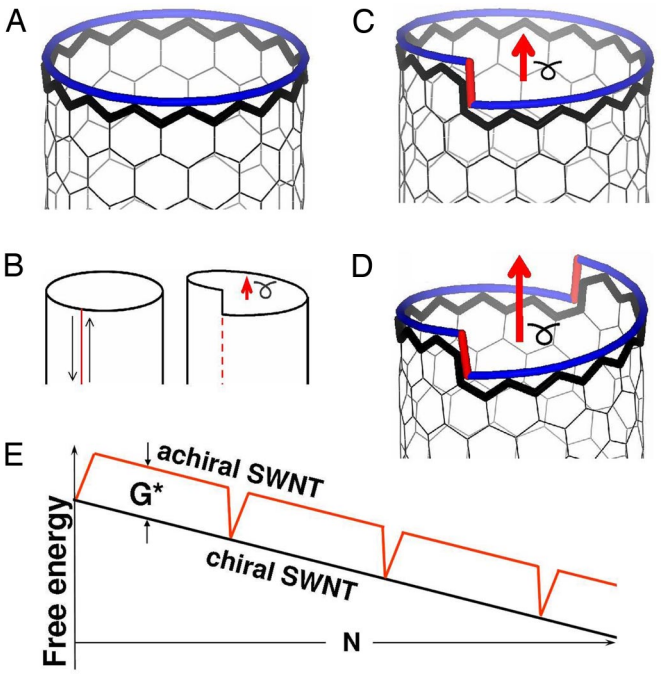

Fig. 1. An axial screw dislocation in the CNT. An achiral zigzag (n, 0) tube (*A*) can be viewed as a perfect crystal, and transformed into a chiral one by cutting, shifting by a Burgers vector **b** (red arrows in *B–D*), and resealing a tube-cylinder (*B*). The chiral (n, 1) in (*C*) and (n, 2) in (*D*) tubes contain the axial screw dislocations with a single and double value of b_γ, accordingly; the corresponding kinks at the open tube-end are marked in red. (*E*) Free energy profile during the growth of a chiral or achiral nanotube.

Author contributions: F.D., A.R.H., and B.I.Y. performed research; B.I.Y. designed research; F.D. and A.R.H. analyzed data; and F.D. and B.I.Y. wrote the paper.

The authors declare no conflict of interest.

Freely available online through the PNAS open access option.

[1]To whom correspondence should be addressed. E-mail: biy@rice.edu.

This article contains supporting information online at www.pnas.org/cgi/content/full/0811946106/DCSupplemental.

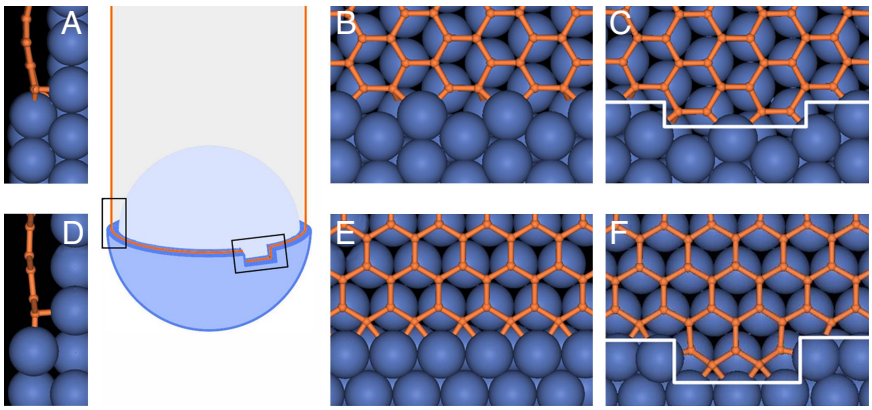

Fig. 2. Nucleation of a next atomic row on the growing tube edge (orange), at the catalyst (blue) surface, is shown as sketch-schematics (center) and in atomistic detail (*A-F*). (*A-C*) An armchair edge near the metal step on Ni (1, 1, 1), its side view (*A*), front view (*B*), and the emerging row segment flanked by the kinks (*C*). Similarly for a zigzag edge (*D-F*), its side view (*D*), front view (*E*), and the emerging nucleus: the row-segment with the end-kinks (*F*), which has higher energy than the armchair case in (*C*). The small left box in the schematics corresponds to the views (*A*) and (*D*) in the direction tangential to the tube wall, while the small right box corresponds to the views (*C*) and (*F*) in the direction normal to the surface.

(Fig. 1*C* and *D*) (*cf.* vicinal surface). Along with this geometrical consideration, it is important to note a qualitative difference from the case of solid bulk or nanowire [which also displays Eshelby twist (20)]. In the last 2 cases, the screw dislocation adds strain, whose energy $\approx|\mathbf{b}|^2$ impedes the larger Burgers vectors (19). In contrast, in a 1-atom-thin CNT wall, the axial screw dislocation carries no energy penalty, thus permitting different magnitudes of $|\mathbf{b}|$ and therefore various chiralities.

The kinks at the end-rim of a chiral tube serve as "cozy corners" (18, 21) for the new atoms docking, while the growth is driven by a monotonous free energy decrease $\Delta G(N) = -\Delta\mu{\cdot}N$ with a number N of added C-atoms (here $\Delta\mu$ is the driving chemical potential drop between the carbon dissolved in the catalyst and its bound state in the tube lattice). Growth of an achiral tube is notably different. Every time its end-edge is complete, an initiation of the next one is needed, with extra energy G^* of under-coordinated carbon at the newly emerging kinks, so that $\Delta G(N) = G^* - \Delta\mu{\cdot}N$. Thus, every time its end-ring (crystal plane) is complete, the achiral tube stumbles upon this re-initiation barrier (Fig. 1*E*). If $G^* > k_bT$, the growth is significantly slower than that for a chiral tube.

Although the armchair tube is similar to zigzag in this respect (both undergoing "complete ring" cycles and both having no chirality by symmetry), there is an important difference in their kinetic behavior: there is not much energy needed to restart each next armchair ring, and in growth it behaves like a chiral tube. To see this and to appreciate the consequences of the above analysis for the growth rate and its overall chirality dependence, it is critical to compute and compare the values of ring-initiation barrier G^*, for the zigzag and armchair tubes. We first note it consists mainly of the energy of 2 terminal kinks at the emerging new layer of atoms. One expects a low barrier for armchair (where such kinks do not add any dangling bonds or obvious distortion) but higher G^* for zigzag (each kink displays an extra dangling bond). This offers partial guidance, but is not directly applicable since the free standing open end of a tube is very unstable due to excessive energy (≈4 eV per triple-bond at armchair and ≈3 eV per dangling bond at zigzag edge), and is prone to closure through the formation of pentagons and curvature. A catalyst mitigates the dangling bond instability and is recognized as necessary to maintain the tube's open end (10). Evaluating the ring-initiation barriers in the presence of metal is less intuitive but can be obtained through direct computations. A graphene (or tube) edge must be docked to a step on the catalyst surface, to avoid its "arch-bridge" warping caused by the tendency of C-metal bonds to stand normal to the metal surface (14, 22, 23). Our DFT calculations confirm this (Fig. S2), and we assess the kink cost G^* from the lower energy and therefore the most realistic "wetted-edge" configuration, where the graphene ends in the metal step (Fig. 2 *A–F*). The emerging-ring nuclei are shown in Fig. 2 *C* and *F*. The kink energies are calculated as the difference between the total energy and the energy of the straight-edge packing of an identical number of atoms (see *Methods* and *SI Text*, Fig. S3).

For an armchair edge on most common catalysts Fe, Co, and Ni, we find $G^*_{AC} = 0.06$, 0.12, and 0.04 eV, respectively. Keeping in mind both the limited accuracy of the computational methods and the high temperature (e.g., typical for CVD growth, $T \approx 1{,}200$ K $\rightarrow$ 0.1 eV), the initiation of an armchair ring has essentially no barrier. In contrast, for a zigzag edge we find $G^*_{ZZ} = 1.41$, 1.12, and 1.54 eV on Fe, Co, and Ni, respectively.

These values show that an armchair tube can grow ring-by-ring almost unobstructed by the difficulties of re-initiation. In this kinetic sense, it can even be viewed as having many kinks along the edge readily accepting new carbon (as Fig. S1*B* illustrates, an "ultimate chiral" tube with $\theta = 30°$). A zigzag tube must wait for fluctuative re-initiation after each atomic ring is complete. The ratio of their growth rates can be roughly estimated as $\exp[-(G^*_{ZZ} - G^*_{AC})/kT] \sim 10^{-4}$–$10^{-6}$ at $T \approx 1{,}200$ K. The initiation rate on a zigzag edge is relatively negligible, and it is rather inert in growth due to high new-ring initiation energy, as we learned from the DFT computations. It can be reiterated here that from a symmetry viewpoint, either zigzag or armchair tubes could be chosen as basic, to introduce a dislocation view for deriving all other chiral types. The barrier computations and consequently different kinetic behavior remove this arbitrariness and unambiguously suggest the more inert zigzag tube as basic. As a result, a clear picture of growth emerges for an arbitrary (n, m) tube. With properties similar to the Frank's dislocation-assisted crystal growth (18), such a tube should readily accrue new C-atoms at the m kinks, at some rate k_0, and thus the total carbon deposition rate is $K = k_0{\cdot}m$. One of the basic characteristics (15) of the CNT is its chiral angle θ [the one between its circumference line and the zigzag motif (Fig. S1)], such that

$$\sin(\theta) = \frac{\sqrt{3}m}{2\sqrt{(m^2 + mn + n^2)}} \sim m/d \sim b_y/d.$$

Thus the carbon deposition rate depends on the chiral angle and tube diameter d as $K \sim k_0{\cdot}d{\cdot}\sin(\theta)$. Finally, the length-speed or the growth rate is,

$$K_l \sim K/d \sim k_0 \cdot \sin(\theta) \propto \theta, \quad [1]$$

where the approximation $\sin(\theta) \approx \theta$ is accurate to 4% for the range of interest, $0 \leq \theta \leq \pi/6$. Upon arriving at this remarkably simple relationship—predicting the amount of CNTs to be proportional to their respective chiral angles—one is compelled to seek its confirmation in experimental data.

Eq. **1** predicts a greater length of nearly armchair tubes relative to rather short and slower growing zigzag. To characterize the tube distribution experimentally it is necessary to unbundle the ropes by sonication (24–29), in the process breaking the tubes into smaller fragments. Because of the fragmentation, greater length translates into a greater number of fragments, i.e., larger abundance.

Before carrying out comparisons with the experimental literature, it is important to recall the basic limitations of the model. Regarding the feedstock decomposition, carbon diffusion across the catalyst to the tube, and its attachment to the end-edge, we assumed the last stage to be limiting. In other words, the microscopic rate constant k_0 is small, although we do not investigate here the exact atomistic mechanism or the activation barrier of this last step. The demonstrated dominance of kink-attachment (no initiation needed) relative to the zigzag-edge (high G^*_{ZZ}) is valid in not-too-hot CVD, but the rate difference may weaken at 3,000–4,000 K of arc-discharge or laser ablation: with the factor of $\exp[-(G^*_{ZZ} - G^*_{AC})/kT] \sim 10^{-1}$–$10^{-2}$ only, the zigzag edge can grow at a comparable rate, making the trend of Eq. **1** less pronounced. Last but not the least, experimental characterization of CNTs by type is usually preceded by additional processing as noted above, which may somewhat alter the distribution of species relative to the as-grown raw material.

With these caveats, Eq. **1** predicts a greater abundance of nearly armchair tubes compared to small amounts or no zigzag. After considering common CNT growth methods, such as various CVD [high pressure carbon monoxide HiPco (24), cobalt-molybdenum catalyzed CoMoCat (25), cobalt-catalyzed on MCM-41 template Co-MCM-41 (26), and ACCVD using alcohol as feedstock (27)], arc discharge (28), and laser ablation (29), we present a composite plot of the chiral angle distribution in Fig. 3. To our surprise, the data from such disparate sources overall follows Eq. **1** well, with HiPco, ACCVD, and arc discharge (28) data fitting Eq. **1** quantitatively, and the CoMoCat data also in good qualitative agreement. Beyond the mere abundance of large chiral angle CNTs, for the HiPco product, Eq. **1** is accurate at each diameter (24), and the detailed ACCVD (27) data show the proportionality $\sim\theta$ unvaried with growth temperature, type of catalyst, or feedstock. Besides the CVD case, the DWNT produced in arc discharge also fit Eq. **1** well, which may indicate that the effective growth temperature in arc discharge does not exceed 2,000 K. Although precise data for Co-MCM41 and laser ablation are not readily available, the semiquantitative data on hand (26, 29) show an abundance of SWNT with large θ, as the theory here predicts. It should be noted that we focus on the steady-state growth of the tube, when ≈99.9% of its body is built, and do not consider the nucleation period, which may possibly discriminate among the CNT types, due to variation in formation energy between the tube and catalyst (3) or preference to certain tube-caps (13). Such nucleation selectivity may account for some deviation of the CoMoCat data from the present theory.

Our model predicts the overall dominance of nearly-armchair material. In the case of a fixed reactor-residence time process (like HiPco), faster growing CNTs individually achieve greater lengths, in proportion to their chiral angles. Presently, due to the lack of corresponding data, we cannot verify this. Thus, this is a prediction to be tested in future experiments.

The above data analysis shows that the present kinetic theory is robust across the various known experiments. Despite its simplicity, it apparently grasps the central features of real processes and must map the way to control CNT chirality during growth—a great challenge in today's nanotube research. If in some implementations, the length of the CNT correlates with the chirality, it possibly provides length as an easier approach to selection. Besides the practical implications, we believe that bridging the nanotube growth and structure on one hand, and the dislocation views in classical crystal growth on the other, should stimulate advances in theory and practice in this important field.

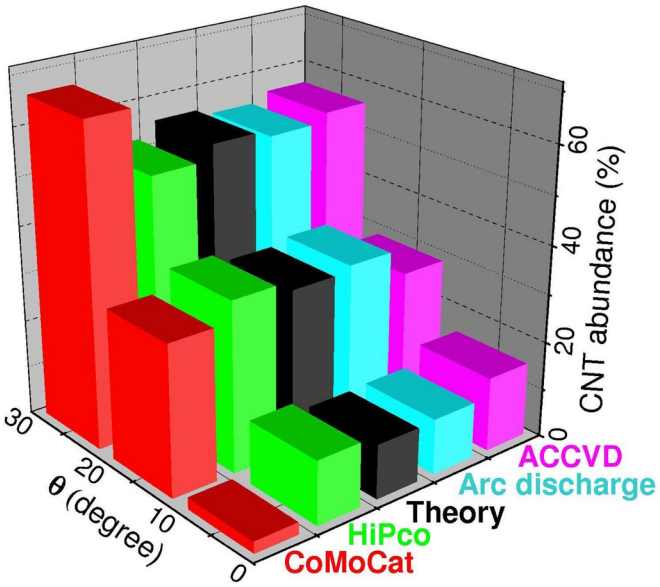

Fig. 3. The distribution of CNT product as a function of chiral angle θ. Experimental data of CoMoCat (25), HiPco (24), arc discharge (28), and ACCVD (27), are extracted from literature. The present model and Eq. **1** predict $N \propto (\theta)$, which yields 11%, 33%, and 56% for the presented intervals (black-gray), to be compared with experimental data (colored).

Methods

Our approach comprised the methods of dislocation theory and the basic notions of nucleation; when we needed to evaluate and compare the energies of certain atomic configurations, we performed the computations with the density functional theory.

The self-consistent DFT calculations were performed to determine the kink formation energy. We used the general gradient approximation (GGA), with the PW91 functional (30), ultra-soft pseudopotential and plane wave basis set. All of the calculations were done with the VASP, Vienna Ab initio Simulation Package (31). The default cutoff energy of 286.74 eV and the convergence stop criteria as the force tolerance $f_{max} < 0.01$ eV/A were used. Due to the large unit cell size, only one *k*-point (Gamma point) was used in the calculation, while additional careful testing is described below.

The (111) metal surface, with or without metal steps, was modeled within the periodic boundary conditions (PBC), with the unit cell 1.4757 nm × 1.278 nm (to attach the zigzag carbon strip/ribbon) or 12.297 nm × 17.34 nm (to attach the armchair carbon strip). Along the *z*-direction perpendicular to the slab surface, the slab was separated by 1.5 nm during the calculation. The metal surface was modeled by a single atomic slab due to the large number of atoms in the unit cell size (≈80–110 atoms per cell, Figs. S2 and S3). During the relaxation, the metal coordinate perpendicular to the metal slab was fixed to avoid unreasonable movement in the *z*-direction. For the surface with the step, 2 extra metal lines were placed on the slab to produce a step configuration (Fig. S3). The graphene strip with an armchair or zigzag edge was attached to the transition metal surface (Fe, Co, and Ni) and fully relaxed by the conjugate gradient (CG) method. For the stepped metal surface, the strip was positioned exactly between the 2 steps.

Without a metal step, the graphene strip tends to form an arch-bridge shape, as shown in Fig. S2. The high curvature and large strain in the ribbon mean that it is not suitable for modeling the kink.

To model the kink formation more realistically, and to mimic the experimental observation and recent theoretical studies (14, 22, 23, 32), the armchair or zigzag strip was attached between the 2 metal steps. In this case, although

the strip buckled up very slightly in the middle, overall it preserved a flat geometry. To create the kinks for their energy evaluation, few C atoms were moved from one to another side, as shown in Fig. S3, with metal atoms rearranged accordingly, forming a total of 4 kinks. Then the formation energy of each kink was calculated as,

$$E_{kink}=(E_2-E_1)/4,$$

where E_1 and E_2 are energies of the perfectly straight strip and the strip with the kinks, respectively.

To support the validity of the used constrained (in the normal z-direction) metal monolayer model and the single $k = 0$ (Gamma-point) calculations, we performed additional computations for 1 case of Ni-metal. Table S1 shows the calculation results based on an unconstrained double metal layer with the Gamma-point ($k = 0$) only or with $2 \times 2 \times 1$ k-points. Because of the great expense of these calculations, only the C-Ni system was studied and only the zigzag case structures were calculated with $2 \times 2 \times 1$ k-points. As shown in Table S1, both the absolute energies and the energy difference found with single k-point and $2 \times 2 \times 1$ k-points agree with each other very well. Similar to the constrained monolayer calculation, the fully-relaxed double layer model shows that the nucleation barrier on an armchair edge is negligible (0.03 eV, similar to 0.04 eV calculated with the z-frozen monolayer model) and the nucleation barrier on a zigzag edge (1.36 eV, similar to the 1.54 eV based on the monolayer model) remains significantly larger than the thermal activation energy k_bT.

ACKNOWLEDGMENTS. This work was supported by the National Science Foundation, the Robert A. Welch Foundation, and the Department of Defense High Performance Computing Center facilities.

1. Iijima S, Ajayan PM, Ichihashi T (1992) Growth model for carbon nanotubes. *Phys Rev Lett* 69:3100–3103.
2. Iijima, S (1993) Growth of carbon nanotubes. *Mat. Sci. & Engin* B19:172–180.
3. Thess A, *et al.* (1996) Crystalline ropes of metallic nanotubes. *Science* 273:483–487.
4. Maiti A, Brabec CJ, Roland CM, Bernholc J (1994) Growth energetics of carbon nanotubes. *Phys Rev Lett* 73:2468–2471.
5. Saito Y (1995) Nanoparticles and filled nanocapsules. *Carbon* 33:979–988.
6. Kiang, C-H, Goddard WA (1996) Polyyne ring nucleus growth model for single-layer carbon nanotubes. *Phys Rev Lett* 76:2515–2518.
7. Charlier, J-C, Vita AD, Blase X, Car R (1997) Microscopic growth mechanisms for carbon nanotubes. *Science* 275:646–649.
8. Lee YH, Kim SG, Tomanek D (1997) Catalytic growth of single-wall carbon nanotubes: an *ab initio* study. *Phys Rev Lett* 78:2393–2396.
9. Fan X, *et al.* (2003) Nucleation of single-walled carbon nanotubes. *Phys Rev Lett* 90:145501.
10. Ding F, *et al.* (2008) The importance of strong carbon-metal adhesion for catalytic nucleation of single-walled carbon nanotubes. *Nano Lett* 8:463–468.
11. Raty, J-Y, Gygi F, Galli G (2005) Growth of carbon nanotubes on metal nanoparticles: A microscopic mechanism from *ab initio* molecular dynamics simulations. *Phys Rev Lett* 95:096103.
12. Yazyev OV, Pasquarello A (2008) Effect of metal elements in catalytic growth of carbon nanotubes. *Phys Rev Lett* 100:156102.
13. Li L, Reich S, Robertson J (2006) Modelling the nucleation and chirality selection of carbon nanotubes. *J Nanosci Nanotech* 6:1290–1297.
14. Abild-Pedersen F, Nørskov JK, Rostrup-Nielsen JR, Sehested J, Helveg S (2006) Mechanisms for catalytic carbon nanofiber growth studied by ab initio density functional theory calculations. *Phys Rev B* 73:115419.
15. Dresselhaus MS, Dresselhaus G, Avouris P (2001) *Carbon Nanotubes* (Springer-Verlag, Heidelberg).
16. Yakobson BI (1998) Mechanical relaxation and 'Intramolecular Plasticity' in carbon nanotubes. *Appl Phys Lett* 72:918–920.
17. Ding F, Jiao K, Lin Y, Yakobson BI (2007) How evaporating carbon nanotubes retain their perfection? *Nano Lett* 7:681–684.
18. Burton WK, Cabrera N, Frank FC (1949) Role of dislocations in crystal growth. *Nature* 163:398–399.
19. Hirth, JP, Lothe J (1982) *Theory of Dislocations* (Wiley, New York).
20. Bierman MJ, Lau YKA, Kvit AV, Schmitt AL, Jin S (2008) Dislocation-driven nanowire growth and Eshelby twist. *Science* 320:1060–1063.
21. Watson, JD (1980) *The Double Helix* (Norton & Co., New York). p 69.
22. Helveg S, *et al.* (2004) Atomic-scale imaging of carbon nanofibre growth. *Nature* 427:426–429.
23. Rodriguez-Manzo JA, *et al.* (2007) In situ nucleation of carbon nanotubes by the injection of carbon atoms into metal particles. *Nature Nano* 2:307-311.
24. Bachilo SM, *et al.* (2002) Structure-assigned optical spectra of single-walled carbon nanotubes. *Science* 298:2361–2366.
25. Bachilo SM, *et al.* (2003) Narrow (n,m)-distribution of single-walled carbon nanotubes grown using a solid supported catalyst. *J Am Chem Soc* 125:1186–1187.
26. Luo Z, Pfefferle LD, Haller GL, Papadimitrakopoulos F (2006) (n,m) abundance evaluation of single-walled carbon nanotubes by fluorescence and absorption spectroscopy. *J Am Chem Soc* 128:15511–15516.
27. Miyauchi Y, Chiashi S, Murakami Y, Hayashida Y, Maruyama S (2004) Fluorescence spectroscopy of single-walled carbon nanotubes synthesized from alcohol. *Chem Phys Lett* 387:198–203.
28. K. Hirahara, *et al.* (2006) Chirality correlation in double-wall carbon nanotubes as studied by electron diffraction. *Phys Rev B* 73:195420.
29. Bandow S, *et al.* (1998) Effect of the growth temperature on the diameter distribution and chirality of single-wall carbon nanotubes. *Phys Rev Lett* 80:3779–3782.
30. Perdew JP, *et al.* (1992) Atoms, molecules, solids, and surfaces: Applications of the generalized gradient approximation for exchange and correlation. *Phys. Rev. B* 46:6671–6687.
31. Kresse G, Hafner J (1993) Ab initio molecular dynamics for liquid metals. *Phys Rev B* 47:558–561.
32. Zhu HW, *et al.* (2005) Atomic-resolution imaging of the nucleation points of single-walled carbon nanotubes. *Small* 1:1180–1183.